crystals

MDPI

Article

# Heterogeneous Crystal Nucleation from the Melt in Polyethylene Oxide Droplets on Graphite: Kinetics and Microscopic Structure

**Muhammad Tariq, Thomas Thurn-Albrecht and Oleksandr Dolynchuk ***

Institute of Physics, Martin Luther University Halle-Wittenberg, 06120 Halle, Germany; muhammad.tariq@physik.uni-halle.de (M.T.); thomas.thurn-albrecht@physik.uni-halle.de (T.T.-A.)
* Correspondence: oleksandr.dolynchuk@physik.uni-halle.de

**Abstract:** It is well known that the crystallization of liquids often initiates at interfaces to foreign solid surfaces. In this study, using polarized light optical microscopy, atomic force microscopy (AFM), and wide-angle X-ray scattering (WAXS), we investigate the effect of substrate–material interactions on nucleation in an ensemble of polyethylene oxide (PEO) droplets on graphite and on amorphous polystyrene (PS). The optical microscopy measurements during cooling with a constant rate explicitly evidenced that the graphite substrate enhances the nucleation kinetics, as crystallization occurred at approximately an 11 °C higher temperature than on PS due to changes in the interactions at the solid interface. This observation allowed us to conclude that graphite induces heterogeneous nucleation in PEO. By employing the classical nucleation theory for analysis of the data with reference to the amorphous PS substrate, the obtained results indicated that the crystal nuclei with contact angles in the range of 100–117° were formed at the graphite interface. Furthermore, we show that heterogeneous nucleation led to a preferred orientation of PEO crystals on graphite, whereas PEO crystals on PS had isotropic orientation. The difference in crystal orientations on the two substrates was also confirmed with AFM, which showed only edge-on lamellae in PEO droplets on graphite compared to unoriented lamellae on PS.

**Keywords:** semicrystalline polymers; droplets; heterogeneous nucleation; homogeneous nucleation; classical nucleation theory; substrates

check for updates

**Citation:** Tariq, M.; Thurn-Albrecht, T.; Dolynchuk, O. Heterogeneous Crystal Nucleation from the Melt in Polyethylene Oxide Droplets on Graphite: Kinetics and Microscopic Structure. *Crystals* **2021**, *11*, 924. https://doi.org/10.3390/cryst11080924

Academic Editor: Andrónico Neira-Carrillo

Received: 1 July 2021
Accepted: 2 August 2021
Published: 9 August 2021

**Publisher's Note:** MDPI stays neutral with regard to jurisdictional claims in published maps and institutional affiliations.

**Copyright:** © 2021 by the authors. Licensee MDPI, Basel, Switzerland. This article is an open access article distributed under the terms and conditions of the Creative Commons Attribution (CC BY) license (https://creativecommons.org/licenses/by/4.0/).

## 1. Introduction

The crystallization of liquids typically starts at interfaces to foreign solid surfaces, such as substrates, the walls of containers, or small particles, e.g., impurities or nucleating agents. In general, a solid substrate can induce the crystallization of liquids either by heterogeneous nucleation [1,2] or by prefreezing [3,4]. Prefreezing, i.e., the formation of a stable crystalline layer at the substrate interface above the melting temperature ($T_m$) of the material, is an equilibrium phenomenon and does not require a nucleation event [5–9]. By contrast, heterogeneous nucleation is an activated process taking place at a finite supercooling below $T_m$ [10]. Under these conditions, the classical path of crystallization occurs in two principal steps: nucleation, which is the formation of small crystal nuclei, and the growth of crystals from the already formed nuclei. If the crystal nuclei are formed within the bulk liquid phase, the corresponding process is called homogeneous nucleation, whereas the formation of crystal nuclei at the foreign surfaces is called heterogeneous nucleation [1,11].

While epitaxy has been known as an important parameter that significantly increases the nucleation rate [12–14], recent in situ atomic force microscopy (AFM) studies showed the occurrence of prefreezing in such epitaxial systems [5–8]. Nevertheless, in the case of heterogeneous nucleation, the effects of the substrate in enhancing the nucleation kinetics are seen as an increase in the density of nucleation events [15] and, thus, as an increase

in the crystallization temperature compared to homogeneous nucleation [16,17]. It has been shown that an elegant method for the experimental study of nucleation is confining the sample into small compartments or droplets [18]. This approach allows for investigating the nucleation kinetics and is widely applied in the studies of crystal nucleation in many different systems, including metals [18,19], water [20–22], and semicrystalline polymers [16,17,23,24]. Especially for semicrystalline polymers, crystallization under confinement is extensively explored by confining polymers into the cylindrical nanopores of alumina [25–27], within nanodomains of block copolymers [28,29], and into dewetted droplets [16,17,23,24]. These confined samples were mainly characterized by differential scanning calorimetry (DSC) [25–27,29], X-ray scattering [25,27,29], AFM [24,28], and optical microscopy [16,17,23,24]. Of particular relevance are the experiments on the dewetted polyethylene oxide (PEO) droplets on amorphous as well as semicrystalline polystyrene (PS) substrates [16,23,24]. On amorphous PS, homogeneous nucleation in PEO droplets was observed, and it was shown that the nucleation rate in that case depends on the volume of droplets [23]. In the case of the semicrystalline PS substrate [24], where the surface roughness of the substrate was varied by applying different thermal treatments, it was found that the nucleation mechanism changes from homogeneous nucleation to heterogeneous nucleation without epitaxy. The corresponding nucleation rate was shown to depend on the base area of droplets. Moreover, the enhanced crystallization kinetics due to heterogeneous nucleation resulted in an increase of the crystallization temperature as compared to that due to homogeneous nucleation. However, estimation of the energetics of heterogeneous nucleation and the microscopic structural analysis of droplets has not been reported until now. There also exists significant interest in identifying the material parameters and potential surfaces, which can enhance crystallization kinetics as well as promote desired crystal morphologies and orientations [10,30].

In this work, we investigated the effects of the substrate–material interactions on crystal nucleation and crystal orientation in an ensemble of PEO droplets formed via dewetting of thin films in the molten state on highly oriented pyrolytic graphite (HOPG) and amorphous PS substrates using optical microscopy, wide-angle X-ray scattering (WAXS), and AFM. Note that the surface of HOPG is atomically flat, apart from the step bunches. According to recent literature reports [20], crystallization from the melt is insensitive to such surface steps, which can mainly affect crystallization from the solution or vapor phase. In this regard, we assume that the step bunches on the HOPG surface do not play any role in our experiments, which allows studying just the effects of the substrate–material interactions. As mentioned above, amorphous PS has no effect on crystallization of PEO [23]. Therefore, PEO droplets on PS act as a reference system in this study used to visualize and quantify the nucleating effects of HOPG on the crystallization of PEO droplets. Our results show that HOPG enhanced the crystallization kinetics of PEO, which resulted in an increase of crystallization temperature by about 11 °C compared to PS during cooling with a constant rate. The latter results allow concluding that PEO on HOPG crystallizes via heterogeneous nucleation. The quantitative analysis of the optical microscopy data with the classical nucleation theory [1] indicates that the PEO crystal nuclei with contact angles in the range of 100–117° were formed at the HOPG interface. Using WAXS and AFM, we show that HOPG induced a preferred crystal orientation in PEO droplets.

## 2. Theory

The classical nucleation theory [1] is a well-known model used to describe nucleation. Nucleation is an activated process, as a crystal nucleus has to overcome an energy barrier ($\Delta G^*$) to become stable and, subsequently, to grow into the bulk phase. A central result of the theory is the analysis of the maximum height of the energy barrier and the corresponding nucleation rate. The latter can be expressed as follows:

$$J = J_o \cdot exp\left(-\frac{\Delta G^*}{k_B T}\right), \quad (1)$$

where $k_B$ is the Boltzmann constant and $T$ is the absolute temperature. The exponential factor in Equation (1) varies much more rapidly with temperature than the prefactor $J_o$, and therefore $J_o$ is often taken to be a constant parameter for a given system [1]. This means that the nucleation rate, as given by Equation (1), depends mainly on the energy barrier for nucleation. In the case of homogeneous nucleation, the nucleus is assumed to have a spherical shape and the corresponding energy barrier $\Delta G^*_{\text{hom}}$ can be expressed as

$$\Delta G^*_{\text{hom}} = \frac{16\pi}{3} \frac{\gamma_{cm}^3 T_m^2}{\Delta H_m^2} \cdot \left( \frac{1}{T_m - T} \right)^2, \tag{2}$$

where $\gamma_{cm}$ is the interfacial free energy at the crystal–melt interface, $T_m$ is the melting temperature, and $\Delta H_m$ is the melting enthalpy. In the case of heterogeneous nucleation on a flat substrate, the nucleus is assumed to have a shape of a spherical cap with a certain non-zero contact angle $\theta$ with the substrate. Compared to homogeneous nucleation, a solid substrate can decrease the energy barrier by a factor $f(\theta)$:

$$\Delta G^*_{\text{het}} = \Delta G^*_{\text{hom}} \cdot f(\theta) \tag{3}$$

where $\Delta G^*_{\text{het}}$ is the energy barrier for heterogeneous nucleation and

$$f(\theta) = \frac{(2 + \cos\theta) \cdot (1 - \cos\theta)^2}{4}. \tag{4}$$

The value of $\theta$ of the crystal nuclei is determined by the interfacial free energies at the interface substrate-melt ($\gamma_{sm}$), substrate-crystal ($\gamma_{sc}$), and crystal–melt ($\gamma_{cm}$) according to Young's equation $\gamma_{sm} = \gamma_{sc} + \gamma_{cm} \cos\theta$. The angle $\theta$ takes a value larger than 90° when $\gamma_{sm} < \gamma_{sc}$, i.e., the substrate prefers to be wetted by the melt phase than by the crystalline phase. If the substrate has an opposite energetic preference, that is, $\gamma_{sm} > \gamma_{sc}$, the value of $\theta$ becomes smaller than 90°. For the both situations, $\gamma_{sm}$ remains overall smaller than the sum $\gamma_{sc} + \gamma_{cm}$. Note that when $\gamma_{sm} > \gamma_{sc} + \gamma_{cm}$, the contact angle $\theta$ becomes zero and $f(0) = 0$ (Equation (4)), implying that the energy barrier for heterogeneous nucleation ($\Delta G^*_{\text{het}}$) vanishes. Under this condition, crystallization can even take place above $T_m$ via prefreezing [3,5–9], the other phenomenon of interface-induced crystallization, which is beyond the framework of classical nucleation theory. For heterogeneous nucleation, $\theta$ has a value $0 < \theta < 180°$ and the function $0 < f(\theta) < 1$. Thus, according to Equation (3), the energy barrier for heterogeneous nucleation $\Delta G^*_{\text{het}}$ is always smaller than that of homogeneous nucleation at a given temperature. This lowered energy barrier for heterogeneous nucleation leads to a decrease in supercooling needed to initiate the nucleation events, as demonstrated in the schematic illustrations in Figure 1, which displays logarithm of normalized nucleation rate $ln(J/J_o)$ as a function of supercooling $(T_m - T)$ for homogeneous and heterogeneous nucleation according to Equations (1)–(3).

As shown in Figure 1, because of the high nucleation barrier at small supercooling, the nucleation rate is negligibly small or practically zero. The homogeneous nucleation events start to take place at a larger supercooling, at which the corresponding nucleation rate rises. On the other hand, the heterogeneous nucleation rate starts to increase at a supercooling smaller than that needed for homogeneous nucleation. As illustrated by the dashed horizontal and vertical lines in Figure 1, the same value of $ln(J/J_o)$ for heterogeneous and homogeneous nucleation corresponds to the different values of $(T_m - T)$. The latter condition, according to Equation (1), reads as follows

$$\frac{\Delta G^*_{\text{het}}}{k_B T_{\text{het}}} = \frac{\Delta G^*_{\text{hom}}}{k_B T_{\text{hom}}}, \tag{5}$$

where $T_{\text{het}}$ is heterogeneous nucleation temperature and $T_{\text{hom}}$ is homogeneous nucleation temperature for a given sample volume during cooling with a constant cooling rate. Sub-

stituting Equation (3) taken at $T = T_{\text{het}}$ and Equation (2) taken at $T = T_{\text{hom}}$ in Equation (5) yields

$$f(\theta) = \frac{T_{\text{het}} \cdot (T_m - T_{\text{het}})^2}{T_{\text{hom}} \cdot (T_m - T_{\text{hom}})^2} \tag{6}$$

Thus, as given by Equation (6), the amounts of supercooling needed to initiate homogeneous and heterogeneous nucleation in a fixed sample volume during the cooling experiments with a constant rate can give information about the factor $f(\theta)$. Furthermore, as Equations (4) and (6) allow accessing the value of $\theta$, the amount of supercooling can be taken as a direct measure of the influence of the interfacial free energies at the substrate interface in enhancing the kinetics of heterogeneous nucleation compared to that of homogeneous nucleation. In this regard, an ensemble of droplets on a solid substrate is a model system, since the time scale for crystal nucleation is much longer than the time scale for crystal growth to detectable sizes, and therefore the nucleation events can be instantly detected [23]. Moreover, as each individual droplet behave like an independent sample and requires a separate nucleation event for crystallization, the simultaneous monitoring of several tens of nucleation events is possible.

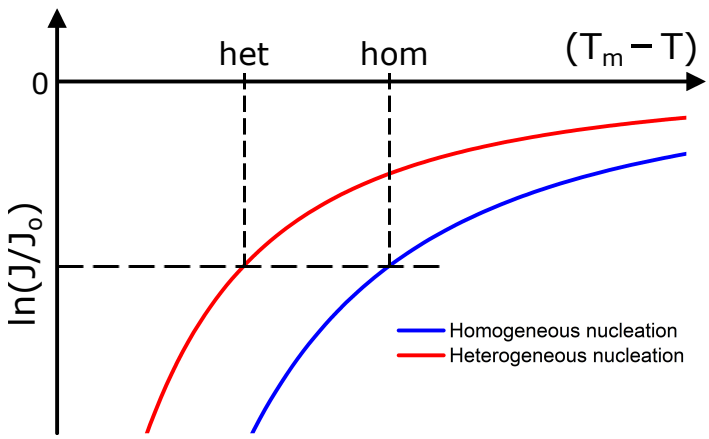


**Figure 1.** Sketches of logarithms of the normalized nucleation rate as a function of supercooling $(T_m - T)$ for homogeneous nucleation (blue curve) and heterogeneous nucleation with a contact angle $\theta = 90°$ (red curve) according to Equations (1)–(3). Dashed horizontal and vertical lines indicate that the same value of $ln(J/J_o)$ for heterogeneous and homogeneous nucleation corresponds to the different values of $(T_m - T)$ during cooling at a given cooling rate for a fixed sample volume.

## 3. Materials and Methods

### *3.1. Materials*

PEO with a molecular weight of $M_w$ = 32,500 g mol $^{-1}$ and PDI = 1.04 was purchased from Polymer Source Inc. The bulk melting temperature $T_m$ of PEO is 64 °C, as measured by DSC (Figure S1). HOPG substrates of quality ZYB were purchased from NT-MDT (Moscow, Russia). For thickness measurements and for preparation of the amorphous PS substrates, silicon wafers ($Si/SiO_2$) purchased from Siegert Wafer (Aachen, Germany) were used. PS of $M_w$ = 192,000 g mol $^{-1}$ was purchased from Sigma Aldrich (Germany). The amorphous PS substrates were prepared by spin coating a 2 wt% solution of PS in toluene onto the cleaned $Si/SiO_2$ wafers at 2000 rpm for 60 s. The resulting films had thickness of about 110 nm, as measured by AFM. The spin-coated PS films were kept in a vacuum oven at 40 °C for 3 h to evaporate any solvent residue. The temperature was then raised to 115 °C for 12 h and slowly cooled down to room temperature.

### *3.2. Sample Preparation*

PEO thin films were prepared by spin coating a solution of PEO in acetonitrile on the freshly cleaved HOPG and PS substrates at 2000 rpm for 60 s. Spin-coated films were kept in a vacuum oven at 40 °C for 3 h for solvent evaporation. The temperature was

subsequently raised to 95 °C for 30 min and then slowly cooled down to room temperature at a cooling rate of about 1 °C min$^{-1}$. Spin-coated films in the molten state at elevated temperatures (above $T_m$) dewet from the two substrates and form isolated droplets. To prepare droplets with the desired size distribution, initial thicknesses of the spin-coated films were adjusted by varying the concentration of polymer in solvent (2 wt% for 60 nm and 2.4 wt% for 80 nm). Thicknesses were determined with AFM on films prepared in the same way on the $Si/SiO_2$ wafers. Droplets formed via the dewetting of a 60 nm thin film on HOPG and a 80 nm thin film on PS had comparable length scales. The base area of droplets ranged from 16 to 262 µm$^2$ on HOPG and from 14 to 338 µm$^2$ on PS, as determined with optical microscopy. The analysis of the base area of PEO droplets on the two substrates is shown in Figure S2. The average values of the contact angles of molten PEO droplets on HOPG and PS were ca. 26° and 31°, respectively, as determined by net-attractive AFM and explained in Figure S3. By using the values of base area and contact angles, the droplet volume can be calculated by assuming the shape of droplets as a spherical cap. The calculated volumes of PEO droplets were in the range from 4 to 274 µm$^3$ on HOPG and 4 to 466 µm$^3$ on PS. As shown in Figure S2, except for only nine large droplets on PS, most of the droplets on the two substrates had a similar base area and, thus, comparable volume. Therefore, we chose PEO droplets formed via dewetting of a 60 nm thin film on HOPG and 80 nm thin film on PS for our experiments.

### *3.3. Optical Microscopy*

Optical microscopy measurements were performed using an Olympus BX51 microscope equipped with an Olympus XC30 camera allowing observation of the sample and recording of the images. A Linkam hotstage equipped with a Linkam TP 94 temperature controller and a Linkam LNP liquid nitrogen controller was used as the sample stage. For the measurements, the samples were placed on the Linkam hotstage, which was then flushed once with nitrogen gas and sealed. The temperature was raised to 85 °C for 15 min and then slowly cooled at a cooling rate of 0.4 °C min$^{-1}$ to −20 °C using a continuous flow of liquid nitrogen. The crystallization in droplets was directly monitored using polarized light optical microscopy, where the positions of the polarizers were kept nearly crossed relative to each other. Under the nearly crossed polarizers, amorphous droplets appear dark and crystal droplets appear bright due to birefringence. Once crystallization in PEO droplets started, a sequence of images was taken after every 0.4 °C decrease in temperature. Olympus Stream Motion software was used to observe the camera view on a computer and to analyze the images.

### *3.4. Atomic Force Microscopy*

AFM measurements were performed at room temperature using an atomic force microscope NanoWizard 4 from JPK instruments (Berlin, Germany). To observe the semicrystalline morphology, the measurements were performed in the net-repulsive regime of operation of intermittent contact mode using NSC 15 cantilevers ($k = 40\,\mathrm{N\,m^{-1}}$, $\omega_o = 325\,\mathrm{kHz}$), purchased from Mikromasch. The cantilever was operated at an excitation frequency $\omega < \omega_o$ and a free amplitude of about 1.6 V. Whereas, to determine the contact angles of liquid PEO droplets on the two substrates, measurements were performed in net-attractive regime of intermittent contact mode [31] at room temperature after cooling the samples from the melt using a heatable sample stage (JPK HTST). For these net-attractive AFM measurements, a soft RFESP-75 cantilever ($k = 3\,\mathrm{N\,m^{-1}}$, $\omega_o = 75\,\mathrm{kHz}$), purchased from Bruker, was employed at an excitation frequency $\omega > \omega_o$ and a free amplitude of about 0.7 V. The open-source software Gwyddion [32] was used to edit and analyze the AFM images.

### *3.5. X-ray Scattering*

Two-dimensional wide-angle X-ray scattering (WAXS) patterns were measured using a SAXSLAB laboratory setup (Retro-F) (Copenhagen, Denmark) equipped with an AXO microfocus X-ray source (Dresden, Germany), an AXO multilayer optics (ASTIX) as a

monochromator for the Cu $K_\alpha$ radiation ($\lambda$ = 0.15418 nm) (Dresden, Germany), and a DECTRIS PILATUS3 R 300K detector (Baden-Daettwil, Switzerland). The sample-to-detector distance was kept at around 89 mm. The measurements were performed in the reflection mode in vacuum at room temperature on PEO droplets on the two substrates. The approximate diameter of the substrates is 8 mm. To observe scattering from those PEO lattice planes, which are not exclusively oriented parallel to the substrate, WAXS measurements were performed under grazing incidence conditions at an incidence angle of 0.2°. Such an incident angle is higher than the critical angle $\alpha_c$ of PEO but lower than $\alpha_c$ of HOPG and enabling scattering from PEO only. Measurements were also performed at various other incident angles (up to 12°) to detect any possible out-of-plane reflections corresponding to the PEO lattice planes oriented parallel to the substrate. Detector images were converted into reciprocal space maps of scattering patterns with two components, $q_z$ and $q_r$, being perpendicular and parallel to the sample surface, respectively [33]. Due to the special geometry of the measurement, a certain area of the reciprocal space along the $q_z$ axis is not accessible and appears as a blank arc. Two additional blank vertical strips appear at the positions where two adjacent parts of the detector meet and are inactive regions of the detector. More details about GIWAXS measurements of thin films on solid substrates can be found in [33].

## 4. Results and Discussion

### *4.1. Optical Microscopy Measurements during Cooling*

To confirm that, compared to amorphous PS, an HOPG substrate has an influence on crystallization of PEO droplets, crystallization in droplets was directly monitored using polarized light optical microscopy. The comparison of the nucleating effect of the HOPG substrate on crystallization of PEO droplets with reference to the amorphous PS substrate is presented in Figure 2, which displays the selected polarized light optical microscopy images of PEO droplets on the two substrates at indicated temperatures during cooling from the melt. Selected optical microscopy images at various other temperatures during cooling of both systems, corresponding to the same series of measurements as that presented in Figure 2, are shown in Figures S4 and S5.

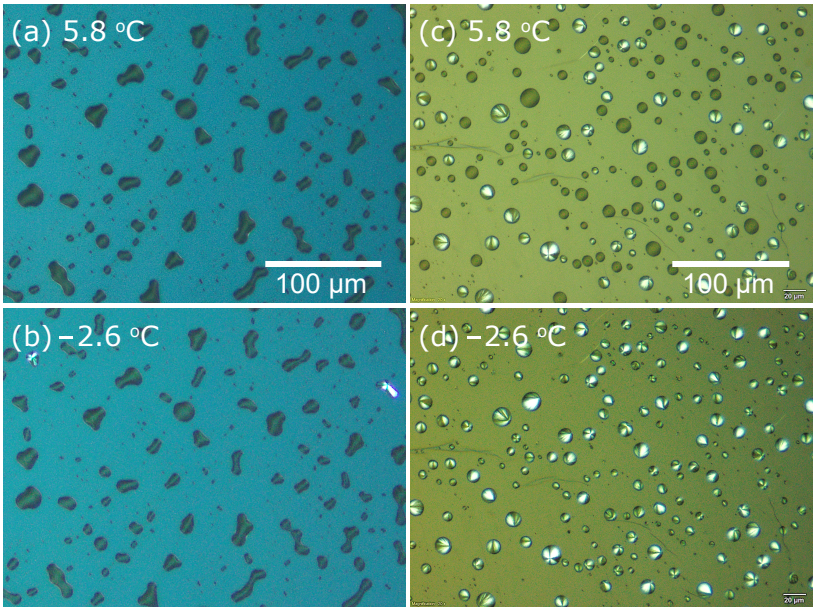


**Figure 2.** Selected optical microscopy images of PEO droplets on (**a**,**b**) PS and (**c**,**d**) HOPG at indicated temperatures during cooling from the melt at a fixed cooling rate of 0.4 °C min$^{-1}$. The position of the polarizers was kept nearly crossed. Selected optical microscopy images at various other temperatures during cooling of the both systems are shown in Figures S4 and S5. The analysis of the base area of droplets can be found in Figure S2.

Although PEO droplets on PS and on HOPG have similar length scales and the experiments were performed under identical conditions, nucleation in PEO droplets occurred in distinctly different temperature ranges on the two substrates. While no nucleation event took place in PEO droplets on PS until 5.8 °C (Figure 2a) during cooling and all droplets were in the liquid phase, many PEO droplets on HOPG were already in a semicrystalline state at the same temperature (Figure 2c). The differences between nucleating activities on the two substrates can be even more prominently seen when the comparison is made at −2.6 °C during cooling. On PS at −2.6 °C (Figure 2b), only two droplets became crystalline, and all other droplets were still in the liquid state. The crystallization of PEO droplets on PS occurred at even lower temperatures (Figure S5). On the other hand, on HOPG at −2.6 °C (Figure 2d), all remaining liquid PEO droplets were crystallized. As mentioned above, the amorphous PS substrate had no nucleating effects on the crystallization of PEO droplets, which crystallized via homogeneous nucleation on PS [16,23,24]. Since PEO droplets are of comparable sizes on the two substrates, the observation of crystallization of PEO droplets at higher temperatures on HOPG compared with on PS (Figure 2) confirms that HOPG enhances the crystallization of PEO droplets. Thereby, we conclude that PEO droplets crystallize via heterogeneous nucleation on HOPG.

To obtain more detailed information about the effects of HOPG on crystallization of PEO droplets, we counted the number of crystalline droplets at each temperature from the series of optical microscopy images obtained during cooling (Figure 2). The results are shown in Figure 3, where the fraction of crystallized droplets, i.e., the ratio of crystalline droplets to the total number of droplets in the image, is plotted as a function of the temperature during cooling.

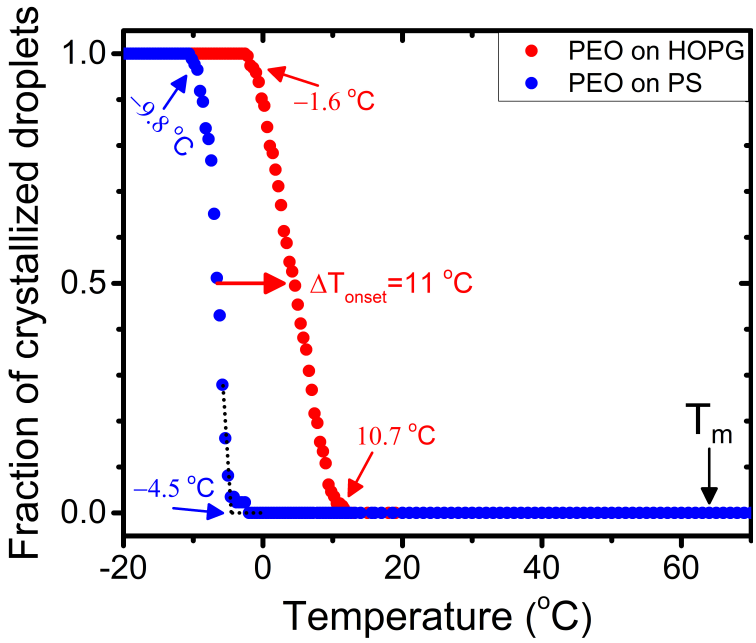


**Figure 3.** Fraction of crystallized PEO droplets on HOPG (red data points) and on PS (blue data points) as a function of temperature during cooling from the melt at a fixed cooling rate of 0.4 °C min$^{-1}$. The back vertical arrow indicates $T_m$ of PEO, and the red horizontal arrow indicates the enhancement in nucleation temperature ($\Delta T_{onset}$) (definition given in the main text) for PEO droplets on HOPG with respect to PS. The other arrows (red for PEO on HOPG and blue for PEO on PS) indicate the temperatures obtained from intercepts of the slopes of linear fits to the data, as once indicated by the dotted lines at the lower part of the data for PEO on PS.

As shown in Figure 3, the droplets remained amorphous on both substrates, and no nucleation event occurred until the samples were cooled far below the melting temperature ($T_m$ = 64 °C). To initiate nucleation, the samples required a sufficient supercooling,

meaning that, a large driving force for crystallization was needed to overcome the energy barrier for nucleation. Once the nucleation events began to take place in droplets on the two substrates, a sharp increase in the fraction of crystallized droplets occurred until all droplets became crystalline. Importantly, the amount of supercooling needed for the occurrence of the nucleation events was different for the two substrates: nucleation occurred at higher temperatures on HOPG than on PS. On PS, the first nucleation event occurred at around −2.6 °C. All droplets in the frame of view on PS became crystalline at around −10.6 °C. This temperature range of the crystallization of PEO droplets on PS is in agreement with the literature reports [16,23,24], where PEO droplets of similar or even somewhat larger sizes on amorphous PS were shown to crystallize approximately between −2 and −7 °C. On the other hand, nucleation in PEO droplets on the HOPG substrate began to take place at around 11.6 °C, and all droplets became crystalline at around −2.6 °C. Here, we define an overall enhancement in the crystallization temperature $\Delta T_{\text{onset}}$ as the temperature difference between the two nucleation curves at the point at which 50% of the total droplets under consideration were crystallized. As shown in Figure 3, HOPG resulted in the enhancement in nucleation in PEO droplets by about 11 °C with reference to the amorphous PS substrate. This amount of enhancement in nucleation temperature by the HOPG substrate represents a notable change in the activation barrier for nucleation [24]. More discussion on the results shown in Figure 3 will appear in the next section, where the data is quantitatively analyzed using the classical nucleation theory.

### *4.2. Quantitative Analysis of Kinetics*

To quantitatively analyze the observed enhanced crystallization kinetics of PEO droplets on HOPG (Figure 3) and to obtain quantitative information about the PEO crystal nuclei formed on HOPG, we employ the classical nucleation theory as introduced in the Theory section. By assuming a similar volume of droplets on the two substrates and using Equation (6), we estimate the value of $f(\theta)$ at the temperatures at which the fraction of crystallized droplets have the value of 0.5 on the HOPG and PS substrates. In addition, since the data points for the two systems follow different slopes, $f(\theta)$ was also evaluated at the temperatures obtained from intercepts of the slopes of linear fits to the data. These temperatures are indicated in Figure 3. In this way, we obtained a possible range of the values of $f(\theta)$. On HOPG, the crystallized droplets fraction of 0.5 corresponded to the temperature of about $T_{\text{PEO-HOPG}} = 4.6$ °C (Figure 3). On PS, the crystallized droplets fraction of 0.5 was achieved at $T_{\text{PEO-PS}} = -6.4$ °C (Figure 3). Substituting the values of $T_{\text{PEO-HOPG}}$ (as the crystallization temperature for heterogeneous nucleation) and $T_{\text{PEO-PS}}$ (as the crystallization temperature for homogeneous nucleation) in Equation (6), we receive $f(\theta) = 0.741$. Similarly, the values of $f(\theta)$ evaluated at the temperatures corresponding to the smallest and highest fractions of crystallized droplets on the two substrates (see the corresponding temperatures in Figure 3) were 0.626 and 0.815, respectively. Thus, according to the classical nucleation theory, the energy barrier for heterogeneous nucleation in PEO droplets on HOPG was 0.626–0.815-times the barrier for homogeneous nucleation on PS. Using the above estimates of $f(\theta)$ and Equation (4), we further estimated the contact angles $\theta$ of crystal nuclei on HOPG. As calculated, the values of $f(\theta)$ of 0.626, 0.741, and 0.815 correspond to the values of contact angle $\theta$ of 99.8°, 109.5°, and 116.8°, respectively. The values of contact angle $\theta$ of the crystal nuclei formed on HOPG were slightly larger than 90°, which, according to Young's equation, implies $\gamma_{sm} < \gamma_{sc}$ and, therefore, indicates that the HOPG substrate had no or even relatively less energetic preference to be wetted by the crystalline phase than by the liquid phase. As will be shown in the next section, even in this situation, heterogeneous nucleation can lead to a preferred crystal orientation. This should not be surprising because the various lattice planes of crystalline material have different energy costs at the substrate interface ($\gamma_{sc}$), and the nucleated lattice plane is presumably the one that costs the least energy.

### 4.3. WAXS and AFM Measurements at Room Temperature

To investigate the influence of HOPG on the crystal orientation and semicrystalline morphology, we performed WAXS and net-repulsive AFM measurements at room temperature on PEO droplets after cooling from 85 °C to −20 °C on HOPG as well as on PS. The results of the WAXS measurements with a 2D detector are shown in Figure 4, which displays the reciprocal space maps of the WAXS pattern of PEO on the two substrates.

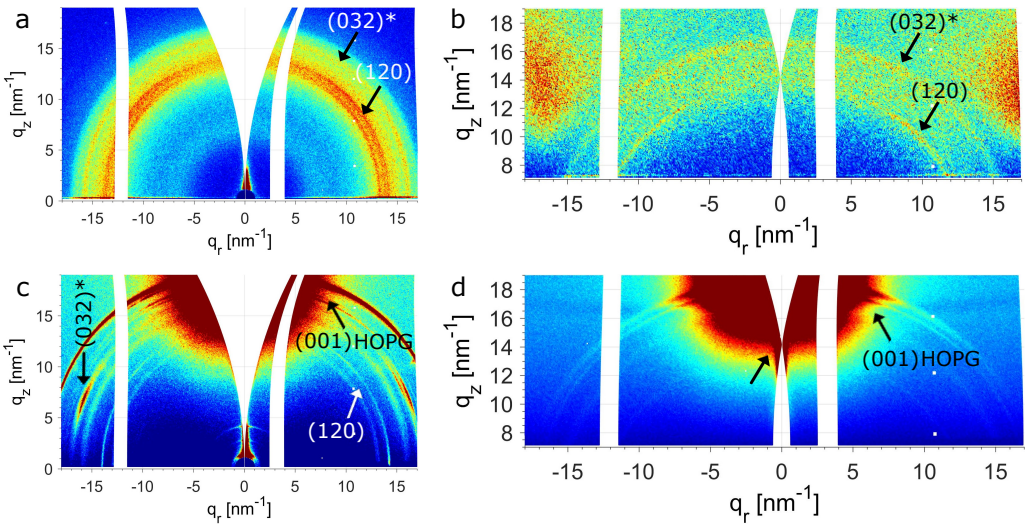


**Figure 4.** Reciprocal space maps of the WAXS pattern of PEO droplets on (**a**,**b**) PS and (**c**,**d**) HOPG measured at room temperature after cooling from the melt to −20 °C. The measurements were performed at the incident angles of (**a**,**c**) 0.2° to observe scattering from those PEO lattice planes, which are not oriented parallel to the substrate and (**b**,**d**) 10° to obtain access to the region of reciprocal space at large $q_z$ values along the substrate normal. All observed reflections are labeled and indicated with the arrows. The unlabeled arrow in (**d**) indicates the region of specular reflection.

As indicated in Figure 4, the dominant (1 2 0) and (0 3 2)* reflections of monoclinic crystal structure of PEO [34] are observed on PS and on HOPG. The (0 3 2)* reflection of PEO is a superimposed signal of many different reflections from the various lattice planes. In Figure 4b, the (1 2 0) and (0 3 2)* reflections appear at around 13.6 nm$^{-1}$ and 16.5 nm$^{-1}$, respectively. The $q$ positions of these reflections correspond well to the scattering pattern of the bulk sample (Figure S6). In the measurements performed under the grazing incidence conditions at an incident angle of 0.2° (Figure 4a), the both reflections from PEO are split into two parts. The $q$ positions of the two split (1 2 0) and (0 3 2)* reflections differ from the expected $q$ positions of both reflections by about ±0.4 nm$^{-1}$. This peak splitting is due to the different sample to detector distance of scattering sites presumably located at the opposite edges on the illuminated area of the sample. The illuminated area of the sample is larger when the incident X-rays reach the sample at shallower angles. At the higher incident angles of X-ray beam, the illuminated area of the sample becomes smaller and does not include the sample edges, and consequently the peak splitting vanishes. Therefore, no peak splitting of the (1 2 0) and (0 3 2)* reflections of PEO was visible in the measurement performed at the incident angle of 10° (Figure 4b) and the both reflections were observed at the expected $q$ positions. As can be seen in Figure 4a,b, the (1 2 0) and (0 3 2)* reflections of PEO are isotropically distributed along the circular arcs. The isotropic distributions of these reflections of PEO on PS indicate that PEO crystals have random orientation on PS, implying that the PS substrate has no orienting effects during crystallization of PEO droplets. This result is anticipated, as PEO droplets on PS crystallize via homogeneous nucleation. By contrast, the WAXS pattern of PEO droplets on HOPG (Figure 4c) is different from that of PEO on PS. First note that the very intense and split scattering signal at around 19.4 nm$^{-1}$ perpendicular to the surface is the reflection from the (0 0 1) lattice planes of HOPG. This reflection covers a large part of the image because of the chosen intensity

scale to make the reflections from PEO visible. The peak splitting of the $(0\,3\,2)^*$ and $(1\,2\,0)$ reflections in Figure 4c is also visible due to the reason mentioned above for PEO on PS. As can be seen in Figure 4c, in addition to the isotropic distribution of the $(1\,2\,0)$ and $(0\,3\,2)^*$ reflections, we also observe one intense and narrowly distributed reflection from the $(0\,3\,2)^*$ lattice planes of PEO. As stated above, the $(0\,3\,2)^*$ reflection is a superposition of many different reflections from various lattice planes. Thus, the narrowly oriented reflection in Figure 4c can be any one of those reflections present within $(0\,3\,2)^*$. However, since the WAXS measurement at the higher incident angle (Figure 4d) is dominated by the strong $(0\,0\,1)$ reflection from HOPG, one could not detect the PEO reflections along the surface normal that would allow us to identify the nucleated lattice planes at the substrate surface. Nevertheless, the presence of the narrowly oriented $(0\,3\,2)^*$ reflection of PEO (Figure 4c) clearly indicates that PEO crystals on HOPG possess a certain preferred crystal orientation with a narrow orientation distribution. This observation demonstrates that the substrate-induced nucleation resulted in a preferred orientation of the crystals.

The aforementioned differences in the orientations of PEO crystals on HOPG and on PS also led to the different semicrystalline morphology of PEO on the two substrates. To visualize these morphological effects, both systems were characterized by net-repulsive AFM measurements at room temperature. Figure 5 shows the results.

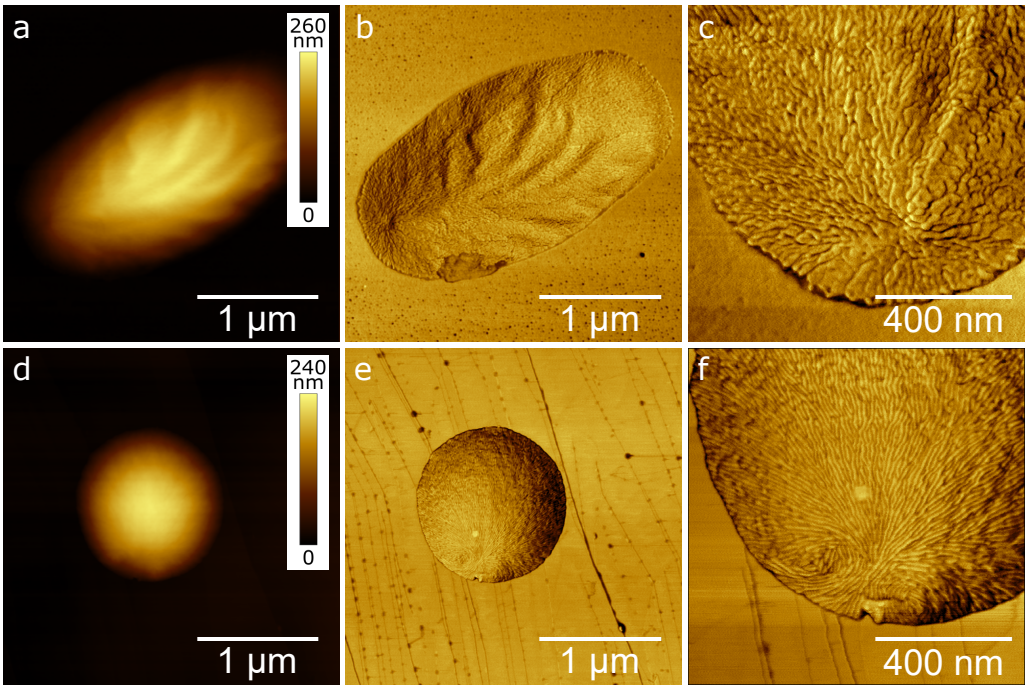


**Figure 5.** Net-repulsive AFM images of PEO droplets at room temperature after cooling from the melt to −20 °C on (**a**–**c**) PS and (**d**–**f**) HOPG. (**a**) AFM height image and (**b**) the corresponding phase image of a PEO droplet on PS. (**c**) Small scale AFM phase image of a part of the same PEO droplet as in a and b. (**d**) AFM height image and (**e**) the corresponding phase image of a PEO droplet on HOPG. (**f**) Small scale AFM phase image of a part of the same PEO droplet as in (**d**,**e**).

AFM height images show the elevated surface of PEO droplets on PS (Figure 5a) and on HOPG (Figure 5d). Bare amorphous surface of the PS substrate is visible around the droplet in the corresponding phase image (Figure 5b). Similarly, the bare surface of HOPG and the step bunches of the HOPG lattice planes are also visible around the PEO droplet in the phase image (Figure 5e). This observation indicates that the PEO droplets are well-isolated from each other, which is essential for droplet-based nucleation experiments, as nucleation in one droplet cannot cause crystallization in the other neighbouring droplets. To resolve the semicrystalline structures in PEO droplets on the two substrates, smaller areas were scanned, in which only a part of the droplet was imaged. A small

scale AFM phase image of the part of the same PEO droplet as in Figure 5a,b is shown in Figure 5c. Similarly, a small scale AFM phase image of the part of the same PEO droplet as in Figure 5d,e is shown in Figure 5f. These small scale AFM phase images show localized nucleation cite and spherulitic structure in PEO droplets on PS (Figure 5c) as well as on HOPG (Figure 5f). However, the different orientations of the lamellae can be identified on the two substrates due to the different substrate–material interactions. On PS, the phase image (Figure 5c) shows unoriented lamellae, whereas only edge-on lamellae are present on HOPG (Figure 5f). Thus, the AFM measurements confirmed that HOPG induces a preferred orientation of lamellar crystals in PEO droplets via heterogeneous nucleation, as a result of the formation of oriented crystal nuclei. Note that no signs of epitaxy between PEO and HOPG are visible in Figure 5f, as the PEO lamellae do not have any strict lateral alignment with respect to the crystallographic directions along the HOPG substrate surface.

The above results of WAXS and AFM measurements provide complementary support to our conclusion that the enhanced crystallization kinetics of PEO droplets on HOPG, shown in Figures 2 and 3, is caused by heterogeneous nucleation.

## 5. Conclusions

In this work, to demonstrate the effects of the substrate–material interactions on nucleation kinetics and the resulting crystal orientation, we investigated crystallization from the melt in an ensemble of PEO droplets with similar base areas on HOPG and amorphous PS substrates. Our results showed that PEO droplets crystallized via heterogeneous nucleation on an HOPG substrate, which led to an increase of the crystallization temperature during cooling at a constant rate by about 11 °C compared to the homogeneous nucleation temperature in PEO droplets on an amorphous PS substrate. By assuming the similar volume of droplets on the two substrates and employing the classical nucleation theory, the contact angles of the PEO crystal nuclei on HOPG were estimated to lie between 100–117°. With the complementary WAXS and AFM measurements, we demonstrated that the substrate-induced nucleation resulted in a preferred orientation of PEO crystals and in edge-on oriented lamellae on HOPG, in contrast to the isotropic crystal orientation of PEO on PS.

In summary, while epitaxy is often considered an important parameter that significantly enhances nucleation kinetics [12–14], we here showed that a solid substrate can enhance the nucleation rate and induce a preferred crystal orientation without epitaxy. Moreover, a comparison of the homogeneous and heterogeneous nucleation rates with the classical nucleation theory can provide quantitative information on the contact angle of crystal nuclei formed at interfaces that is hardly accessible otherwise. The latter enables a direct judgment of the strength of foreign surfaces in inducing the crystal nucleation that is important for numerous applications of semicrystalline polymers. However, it sometimes becomes difficult to distinguish between homogeneous and heterogeneous nucleation. In this respect, our WAXS measurements are also a methodological step forward in studying substrate-induced crystallization and show the ease with which the differentiation between homogeneous and heterogeneous nucleation can be made.

**Supplementary Materials:** The following are available online at https://www.mdpi.com/article/10.3390/cryst11080924/s1, Figure S1: DSC measurement of $T_m$ of PEO, Figure S2: Comparison of base area of PEO droplets on HOPG and PS, Figure S3: Determination of contact angles of molten PEO droplets on HOPG and PS, Figures S4 and S5: Selected additional optical microscopy images of PEO droplets on HOPG and PS at various temperatures during cooling from the melt, and Figure S6: WAXS pattern of bulk PEO.

**Author Contributions:** T.T.-A. designed the research; M.T. performed the research, M.T. and O.D. analyzed and interpreted the data; T.T.-A. participated in discussions; M.T. and O.D. wrote the paper. All authors have read and agreed to the published version of the manuscript.

**Funding:** This research was funded by the Deutsche Forschungsgemeinschaft (DFG, German Research Foundation)—Project-ID 189853844—TRR 102 and European Union (EFRE).

**Institutional Review Board Statement:** Not applicable.

**Informed Consent Statement:** Not applicable.

**Data Availability Statement:** Data are contained within the article and supplementary material.

**Acknowledgments:** The authors acknowledge Wolf Widdra and Erik Schreck for kindly providing various substrates for initial screening experiments. We also thank Katrin Herfurt for the DSC measurements.

**Conflicts of Interest:** The authors declare no conflict of interest.

## References

1. Sear, R. Nucleation: Theory and Applications to Protein Solutions and Colloidal Suspensions. *J. Phys. Condens. Matter.* **2007**, *19*, 033101. [CrossRef]
2. Sosso, G.C.; Chen, J.; Cox, S.J.; Fitzner, M.; Pedevilla, P.; Zen, A.; Michaelides, A. Crystal Nucleation in Liquids: Open Questions and Future Challenges in Molecular Dynamics Simulations. *Chem. Rev.* **2016**, *116*, 7078–116. [CrossRef]
3. Heni, M.; Löwen, H. Surface Freezing on Patterned Substrates. *Phys. Rev. Lett.* **2000**, *85*, 3668–3671. [CrossRef]
4. Courtemanche, D.; Pasmore, T.; Vanswol, F. A Molecular-Dynamics Study of Prefreezing Hard-Spheres at A Smooth Hard-Wall. *Mol. Phys.* **1993**, *80*, 861–875. [CrossRef]
5. Löhmann, A.; Henze, T.; Thurn-Albrecht, T. Direct Observation of Prefreezing at the Interface Melt-Solid in Polymer Crystallization. *Proc. Natl. Acad. Sci. USA* **2014**, *111*, 17368–17372. [CrossRef] [PubMed]
6. Flieger, A.K.; Schulz, M.; Thurn-Albrecht, T. Interface-Induced Crystallization of Polycaprolactone on Graphite via First-Order Prewetting of the Crystalline Phase. *Macromolecules* **2018**, *51*, 189–194. [CrossRef]
7. Tariq, M.; Dolynchuk, O.; Thurn-Albrecht, T. Effect of Substrate Interaction on Thermodynamics of Prefreezing. *Macromolecules* **2019**, *52*, 9140–9148. [CrossRef]
8. Tariq, M.; Dolynchuk, O.; Thurn-Albrecht, T. Independent Variation of Transition Temperature and Prefrozen Layer Thickness at the Prefreezing Transition. *J. Phys. Chem. C* **2020**, *124*, 26184–26192. [CrossRef]
9. Dolynchuk, O.; Tariq, M.; Thurn-Albrecht, T. Phenomenological Theory of First-Order Prefreezing. *J. Phys. Chem. Lett.* **2019**, *10*, 1942–1946. [CrossRef]
10. Bourque, A.; Locker, C.; Rutledge, G. Heterogeneous Nucleation of an n-Alkane on Tetrahedrally Coordinated Crystals. *J. Phys. Chem. B* **2017**, *121*, 904–911. [CrossRef]
11. Schick, C.; Androsch, R.; Schmelzer, J. Homogeneous Crystal Nucleation in Polymers. *J. Phys. Condens. Matter.* **2017**, *29*, 453002. [CrossRef]
12. Wittmann, J.; Lotz, B. Epitaxial Crystallization of Polyethylene on Organic Substrates: A Reappraisal of the Mode of Action of Selected Nucleating Agents. *J. Polym. Sci. Polym. Phys. Ed.* **1981**, *19*, 1837–1851. [CrossRef]
13. Wittmann, J.; Hodge, A.; Lotz, B. Epitaxial Crystallization of Polymers onto Benzoic Acid: Polyethylene and Paraffins, Aliphatic Polyesters, and Polyamides. *J. Polym. Sci. Polym. Phys. Ed.* **1983**, *21*, 2495–2509. [CrossRef]
14. Wittmann, J.; Lotz, B. Epitaxial Crystallization of Polymers on Organic and Polymeric substrates. *Prog. Polym. Sci.* **1990**, *15*, 909–948. [CrossRef]
15. Tong, Y.; Lin, Y.; Wang, S.; Song, M. A Study of Crystallisation of Poly (ethylene oxide) and Polypropylene on Graphene Surface. *Polymer* **2015**, *73*, 52–61. [CrossRef]
16. Massa, M.; Carvalho, J.; Dalnoki-Veress, K. Direct Visualisation of Homogeneous and Heterogeneous Crystallisation in an Ensemble of Confined Domains of Poly(ethylene oxide). *Eur. Phys. J. E* **2003**, *12*, 111–117. [CrossRef]
17. Carvalho, J.; Dalnoki-Veress, K. Surface Nucleation in the Crystallisation of Polyethylene Droplets. *Eur. Phys. J. E* **2011**, *34*, 6. [CrossRef]
18. Vonnegut, B. Variation with Temperature of the Nucleation Rate of Supercooled Liquid Tin and Water Drops. *J. Colloid Sci.* **1948**, *3*, 563–569. [CrossRef]
19. Turnbull, D.; Cech, R.E. Microscopic Observation of the Solidification of Small Metal Droplets. *J. Appl. Phys.* **1950**, *21*, 804–810. [CrossRef]
20. Campbell, J.; Meldrum, F.; Christenson, H. Is Ice Nucleation from Supercooled Water Insensitive to Surface Roughness? *J. Phys. Chem. C* **2015**, *119*, 1164–1169. [CrossRef]
21. Murray, B.J.; Broadley, S.L.; Wilson, T.W.; Atkinson, J.D.; Wills, R.H. Heterogeneous Freezing of Water Droplets Containing Kaolinite Particles. *Atmos. Chem. Phys.* **2011**, *11*, 4191–4207. [CrossRef]
22. Xue, H.; Lu, Y.; Geng, H.; Dong, B.; Wu, S.; Fan, Q.; Zhang, Z.; Li, X.; Zhou, X.; Wang, J. Hydroxyl Groups on the Graphene Surfaces Facilitate Ice Nucleation. *J. Phys. Chem. Lett.* **2019**, *10*, 2458–2462. [CrossRef]
23. Massa, M.; Dalnoki-Veress, K. Homogeneous Crystallization of Poly(ethylene oxide) Confined to Droplets: The Dependence of the Crystal Nucleation Rate on Length Scale and Temperature. *Phys. Rev. Lett.* **2004**, *92*, 255509. [CrossRef]
24. Carvalho, J.; Dalnoki-Veress, K. Homogeneous Bulk, Surface, and Edge Nucleation in Crystalline Nanodroplets. *Phys. Rev. Lett.* **2010**, *105*, 237801. [CrossRef] [PubMed]
25. Shingne, N.; Geuss, M.; Hartmann-Azanza, B.; Steinhart, M.; Thurn-Albrecht, T. Formation, Morphology and Internal Structure of One-Dimensional Nanostructures of the Ferroelectric Polymer P(VDF-TrFE). *Polymer* **2013**, *54*, 2737–2744. [CrossRef]

26. Duran, H.; Steinhart, M.; Butt, H.; Floudas, G. From Heterogeneous to Homogeneous Nucleation of Isotactic Poly(propylene) Confined to Nanoporous Alumina. *Nano Lett.* **2011**, *11*, 1671–1675. [CrossRef] [PubMed]
27. Suzuki, Y.; Duran, H.; Steinhart, M.; Butt, H.J.; Floudas, G. Homogeneous Crystallization and Local Dynamics of Poly(ethylene oxide) (PEO) Confined to Nanoporous Alumina. *Soft Matter* **2013**, *9*, 2621–2628. [CrossRef]
28. Reiter, G.; Castelein, G.; Sommer, J.U.; Röttele, A.; Thurn-Albrecht, T. Direct Visualization of Random Crystallization and Melting in Arrays of Nanometer-Size Polymer Crystals. *Phys. Rev. Lett.* **2001**, *87*, 226101. [CrossRef] [PubMed]
29. Röttele, A.; Thurn-Albrecht, T.; Sommer, J.U.; Reiter, G. Thermodynamics of Formation, Reorganization, and Melting of Confined Nanometer-Sized Polymer Crystals. *Macromolecules* **2003**, *36*, 1257–1260. [CrossRef]
30. Dolynchuk, O.; Schmode, P.; Fischer, M.; Thelakkat, M.; Thurn-Albrecht, T. Elucidating the Effect of Interfacial Interactions on Crystal Orientations in Thin Films of Polythiophenes. *Macromolecules* **2021**, *54*, 5429–5439. [CrossRef]
31. Henze, T.; Schröter, K.; Thurn-Albrecht, T. Investigation of the Different Stable States of the Cantilever Oscillation in an Atomic Force Microscope. *Nanotechnology* **2012**, *23*, 245702. [CrossRef]
32. Nečas, D.; Klapetek, P. Gwyddion: An Open-Source Software for SPM Data Analysis. *Cent. Eur. J. Phys.* **2012**, *10*, 181–188. [CrossRef]
33. Balko, J.; Portale, G.; Lohwasser, R.; Thelakkat, M.; Thurn-Albrecht, T. Surface Induced Orientation and Vertically Layered Morphology in Thin Films of Poly(3-hexylthiophene) Crystallized from the Melt. *J. Mater. Res.* **2017**, *32*, 1957–1968. [CrossRef]
34. Takahashi, Y.; Tadokoro, H. Structural Studies of Polyethers, $(-(CH_2)m-O-)_n$. X. Crystal Structure of Poly(ethylene oxide). *Macromolecules* **1973**, *6*, 672–675. [CrossRef]